



Article

Diatomite-like KFeS_2 for Use in High-Performance Electrodes for Energy Storage and Oxygen Evolution

Can Wang¹, Kailin Li¹, Qing Sun², Shijin Zhu¹, Chenzhi Zhang¹, Yunhao Zhang³, Zhongyi Shi⁴, Youzhong Hu¹ and Yuxin Zhang^{1,*} 

¹ College of Materials Science and Engineering, Chongqing University, Chongqing 400044, China

² Multi-Scale Porous Materials Center, School of Chemistry and Chemical Engineering, Chongqing University, Chongqing 400044, China

³ School of Energy and Power Engineering, Chongqing University, Chongqing 400044, China

⁴ Undergraduate School, Chongqing University, Chongqing 400044, China

* Correspondence: zhangyuxin@cqu.edu.cn

Abstract: Bifunctional materials possess remarkable properties that allow them to store and convert electrical energy easily. In this paper, diatomite-like potassium iron disulfide (KFeS_2) was synthesized by a multistep sacrificial template method, and its morphological, electrochemical, and oxygen evolution reaction (OER) properties were investigated. KFeS_2 was found to be porous, hollow, and cake-like, which suggests a high specific surface area (SSA) and abundant electrochemically active sites. A very high specific capacitance of 651 F g^{-1} at 1.0 A g^{-1} was also obtained due to the substance's unique structure and high porosity. Additionally, the diatomite-like KFeS_2 possessed a very low overpotential η_{10} of 254 mV at a current density of 10 mA cm^{-2} and a small Tafel slope of about 48.4 mV dec^{-1} . Thus, the diatomite-like KFeS_2 demonstrates broad application prospects for both energy storage and conversion.

Keywords: KFeS_2 ; diatomite; hydrothermal synthesis; supercapacitors; oxygen evolution reaction



Citation: Wang, C.; Li, K.; Sun, Q.; Zhu, S.; Zhang, C.; Zhang, Y.; Shi, Z.; Hu, Y.; Zhang, Y. Diatomite-like KFeS_2 for Use in High-Performance Electrodes for Energy Storage and Oxygen Evolution. *Nanomaterials* **2023**, *13*, 643. <https://doi.org/10.3390/nano13040643>

Academic Editor: Byunghoon Kim

Received: 22 December 2022

Revised: 26 January 2023

Accepted: 1 February 2023

Published: 6 February 2023



Copyright: © 2023 by the authors. Licensee MDPI, Basel, Switzerland. This article is an open access article distributed under the terms and conditions of the Creative Commons Attribution (CC BY) license (<https://creativecommons.org/licenses/by/4.0/>).

1. Introduction

Energy storage and conversion are two key points related to many proposed solutions for serious environmental problems to energy production, and both have already received considerable academic attention over the years [1–4]. As a type of electrochemical energy storage device, supercapacitors can be widely used in many “new energy” vehicles, camera flashes, and energy back-up systems because of their higher power density, faster charge and discharge rates, and longer cycle lives compared to conventional batteries [5–7]. In addition, the electrochemical energy conversion pathway of the oxygen evolution reaction (OER), which is one half of the electrochemical decomposition of water, is environmentally friendly, low cost, emits no carbon, and can be used to produce clean hydrogen energy. OER has also already been widely studied, and the performance of supercapacitance and OER relies on the active materials used. Iron-based compounds have been used as a primary electrode material for supercapacitors due to the various valence states of Fe, as well as their high specific capacitance, wide potential window, low cost, and their own environmental friendliness [8,9]. Among them, iron-based sulfides have become one of the most important electrode materials for supercapacitors due to their high electrical conductivity and unique physicochemical properties [10–13]. Furthermore, iron-based sulfide nanomaterials are considered to be efficient electrocatalytic materials due to their high abundance, low toxicity, and high electrochemical activity [14–18].

Among all iron-based compounds, ternary KFeS_2 possesses variable physical and chemical properties because of its mixed-valence Fe [19,20]. Thus, ternary KFeS_2 shows broad application prospects in energy storage and electrocatalysis [21–26]. However, the

electrochemical properties of most KFeS_2 nanostructures are much lower than their theoretical values because of their low specific surface area (SSA) resulting in poor electrochemically active sites [27–29]. Additionally, KFeS_2 has also been found to exhibit the phenomenon of easy agglomeration [21]. Therefore, shaping KFeS_2 into a unique morphology that both prevents agglomeration and enhances its SSA would have immediate benefits.

To this end, as a sacrificial template material, diatomite has become one of the most popular templates for preparing porous structures due to its own high porosity, low volumetric weight, high chemical stability, and high SSA [30,31]. In addition, the three-dimensional structure of diatomite has been shown to be able to solve the problem of material agglomeration effectively [6,32,33]. Thus, in this work, we propose a simple and controllable method for the synthesis of KFeS_2 with diatomite morphology using a multistep sacrificial template.

2. Materials and Methods

All chemicals were purchased from Aladdin (Shanghai, China) and were of analytical purity and thus used without further purification. The diatomite material was also supplied from Aladdin.

2.1. Synthesis of $\text{FeOOH}@D$ Nanorods on Diatomite (D)

$\text{MnO}_2@D$ was prepared by modifying a one-step hydrothermal method that has been previously published by our research group [6]. KMnO_4 solution (70 mL, 0.05 M) and diatomite (100 mg) were placed into a Teflon-lined stainless-steel autoclave (Henan Gongyi Yuhua Instrument Co. LTD, Henan, China) that was subsequently maintained at 160 °C for 24 h. The sample was then removed, washed with distilled water and ethanol, and dried at 60 °C to obtain MnO_2 composites. Subsequently, 150 mg $\text{FeSO}_4 \cdot 7\text{H}_2\text{O}$ and 80 mg $\text{MnO}_2@D$ were dissolved and dispersed in 70 mL of an ethylene glycol–water solution (ethylene glycol:water = 1:7) successively, and the mixture was transferred to a Teflon-lined stainless-steel autoclave and rotated at 120 °C for 12 h. After cooling to room temperature, the product was washed with de-ionized (DI) water and dried at 60 °C for 12 h.

2.2. Synthesis of Diatomite (D)-like KFeS_2

The as-prepared $\text{FeOOH}@D$ (100 mg), $\text{Na}_2\text{S} \cdot 9\text{H}_2\text{O}$ (2.88 g), and KOH (19.6 g) were next dispersed and dissolved in 70 mL of the ethanol–water solution (water: ethanol = 1:1). Then, the mixture was transferred into a Teflon-lined stainless-steel autoclave and rotated constantly at 120 °C for 12 h. After cooling to room temperature, the product was washed with DI water and dried at 60 °C for 12 h.

2.3. Synthesis of FeS_2 -Modified Diatomite

To create the FeS_2 -modified diatomite, the as-prepared $\text{FeOOH}@D$ (100 mg) and $\text{Na}_2\text{S} \cdot 9\text{H}_2\text{O}$ (2.88 g) were dispersed and dissolved in 70 mL of the ethanol–water solution (water:ethanol = 1:1). Then, the mixture was transferred into a Teflon-lined stainless-steel autoclave and constantly rotated at 120 °C for 12 h. After cooling to room temperature, this product was washed with DI water and dried at 60 °C for 12 h.

2.4. Synthesis of KFeS_2

The MnO_2 composites were prepared using a one-step hydrothermal method. As is typical, KMnO_4 solution (70 mL, 0.05 M) was placed into a Teflon-lined stainless-steel autoclave at 160 °C for 24 h. The sample was then removed, washed with distilled water and ethanol, and dried at 60 °C to obtain the MnO_2 composites.

Next, 150 mg $\text{FeSO}_4 \cdot 7\text{H}_2\text{O}$ and 80 mg MnO_2 were then dispersed in 70 mL of an ethylene glycol–water solution (ethylene glycol:water = 1:7) successively. The mixture was subsequently transferred to a Teflon-lined stainless-steel autoclave and rotated constantly at 120 °C for 12 h. After cooling to room temperature, the product was washed with DI water and dried at 60 °C for 12 h.

Finally, the as-prepared FeOOH (100 mg), Na₂S·9H₂O (2.88 g), and KOH (19.6 g) were dispersed and dissolved in 70 mL of the ethanol–water solution (water:ethanol = 1:1), and the mixture was then transferred into a Teflon-lined stainless-steel autoclave and rotated constantly at 120 °C for 12 h. After cooling to room temperature, the product was washed with DI water and dried at 60 °C for 12 h.

2.5. Characterization of Materials

The crystal structures of the KFeS₂ and diatomite-like KFeS₂ were determined by X-ray diffraction (XRD) (Panaco, Almelo, The Netherlands) at a scanning angle of $2\theta = 5\text{--}80$ degrees. The chemical constituents of the samples were determined by X-ray photoelectron spectroscopy (XPS) (Thermo Fisher Technology, Waltham, MA, USA) as well, and the micromorphology and structure were characterized using scanning electron microscopy (SEM) (Zeiss, Germany) at 5 kV and transmission electron microscopy (TEM) (Zeiss, Germany).

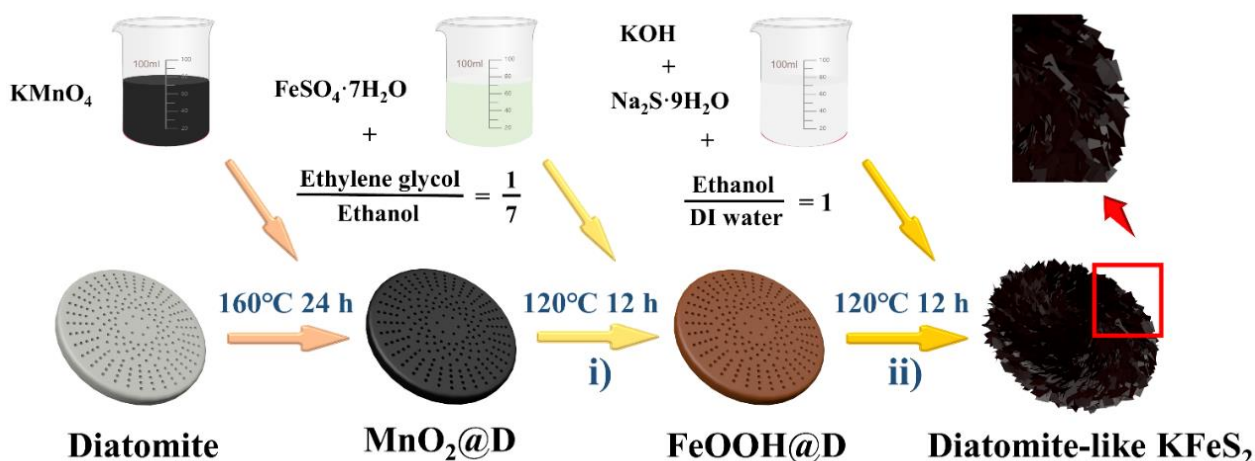
2.6. Electrochemical Measurements

A working electrode was prepared by mixing 70 wt% active materials (diatomite-like KFeS₂), 20 wt% acetylene black, and 10 wt% polyvinylidene fluoride (PVDF) in N-methyl-2-pyrrolidone (NMP), and the slurry was spread onto a foam nickel current collector ($1 \times 1 \text{ cm}^2$). This electrode was then heated to 120 °C for 12 h in order to evaporate the solvent and was then uniaxially pressed under 10 MPa. A three-electrode was then used to evaluate the capacitive performance of the electrode materials.

The electrochemical performance of the as-prepared electrode was carried out using the CHI 660E electrochemical station (Shanghai Chenhua Instrument Co., LTD, Shanghai, China). For the three-electrode configuration, the working electrodes ($1 \times 1 \text{ cm}^2$) were the diatomite-like KFeS₂, a platinum plate was used as the counter electrode, and silver chloride electrode was used as the reference electrode. Cyclic voltammetry (CV), linear sweep voltammetry (LSV), and galvanostatic charging/discharging (GCD) were employed to investigate the electrochemical performance of the composites, where the applied potential window ranged from 0 to 0.6 V in a 6 M KOH electrolyte. CVs were recorded at scan rates of 10, 20, 40, 50, 80, and 100 mV s⁻¹, and GCD curves were obtained at constant current densities of 1, 2, 4, 5, 8, and 10 A g⁻¹. CV and GCD had potential windows of 0.6 V and 0.45 V, respectively. Finally, electrochemical impedance spectroscopy (EIS) was conducted in the frequency range of 100 kHz to 0.01 Hz with a perturbation amplitude of 5 mV versus the open-circuit potential.

3. Results and Discussion

As shown in Scheme 1, the diatomite-like KFeS₂ was synthesized using a sacrificial template method that combined the etching of sulfide and diatomite into one step. In the first step of the process, MnO₂@diatomite (MnO₂@D) was prepared using a hydrothermal method according to the self-decomposition of KMnO₄. Then, the prepared MnO₂ was replaced by hydroxyl iron oxide (FeOOH) based on the spontaneous redox reaction between Fe²⁺ and MnO₂. After becoming vulcanized by Na₂S·9H₂O in the alcohol–water solution under high temperature, FeOOH was transformed into KFeS₂ and the diatomite was dissolved by KOH, resulting in a hollow diatomite-like KFeS₂ structure.



Scheme 1. Multistep sacrificial template method to prepare biomimetic diatomite structured KFeS₂ electrode materials with bifunction of supercapacitance and hydrolysis: (i) Conversion of MnO₂ nanosheets to FeOOH nanorods on the surface of diatomite template; (ii) Etching of diatomite in FeOOH@D template and sulfation of FeOOH by KOH and Na₂S·9H₂O at the same time to prepare diatomite-like KFeS₂.

Figure 1 shows the morphology of diatomite-like KFeS₂. In Figure 1a, after the multistep sacrificial template method, the KFeS₂ also kept a diatomite-like round cake shape that consisted of numerous nanosheets that joined together with each other to form a porous structure (Figure 1b,c). This structure could also be observed inform the TEM images (Figure 1d–f). This unique nanostructure definitely increased the SSA of KFeS₂, which is very important for improving its electrochemical and OER properties. Moreover, a lattice spacing of 0.564 nm, as shown in Figure 1g, can be indexed to the (0 2 0) plane of KFeS₂, and the typical EDS spectrum in Figure 1h reveals that the atomic percentage of elements K, Fe, and S followed a ratio of 1:1:2, which indicates the presence of KFeS₂. Furthermore, the element mapping images and scatter superimposed graph in Figure 1i also show that K, Fe, and S were uniformly distributed in the material. These results point to the successful synthesis of KFeS₂ with the 3D morphology and dimensions of diatomite.

For comparison, FeS₂-modified diatomite was produced but without diatomite etching. Figure 2a shows the composition and crystalline phase of purified diatomite, FeS₂-modified diatomite, and diatomite-like KFeS₂. The diffraction peaks of purified diatomite were observed at 22.0°, 28.4°, 31.5°, and 36.1°, which refer to SiO₂ (JCPDS No. 39-1425, $a = 4.937 \text{ \AA}$, $b = 4.937 \text{ \AA}$, $c = 6.924 \text{ \AA}$), indicating a chemical composition of diatomite. For FeS₂-modified diatomite, only weak diffraction peaks were found for diatomite because the template of diatomite was not etched. However, the diffraction peaks of diatomite-like KFeS₂ were observed as 15.6°, 27.4°, 30.7°, and 40.9° (JCPDS No. 80-0581, $a = 7.089 \text{ \AA}$, $b = 11.304 \text{ \AA}$, $c = 5.398 \text{ \AA}$), demonstrating its high crystallinity, and the average crystallites size is about 27.5 nm. Additionally, the diffraction peaks of purified diatomite could not be observed, which confirmed that the diatomite was completely etched by KOH. Moreover, the sample without etching was also studied and clearly showed that the synthesis of KFeS₂ had occurred as a product of the co-heating of KOH with Na₂S·9H₂O and hydroxy-iron oxide. Figure 2b depicts the FTIR spectrum of the diatomite-like KFeS₂. The peak at 3420 cm⁻¹ corresponds to strong stretching vibrations of the O–H bond (H₂O), and the bands at 1126 cm⁻¹ and 829 cm⁻¹ correspond to the asymmetric stretching of sulfur functional groups (S–O). Finally, the peaks at 708 cm⁻¹, 665 cm⁻¹, 614 cm⁻¹, and 539 cm⁻¹ correspond to disulfide stretching vibrations (S–S) [34].

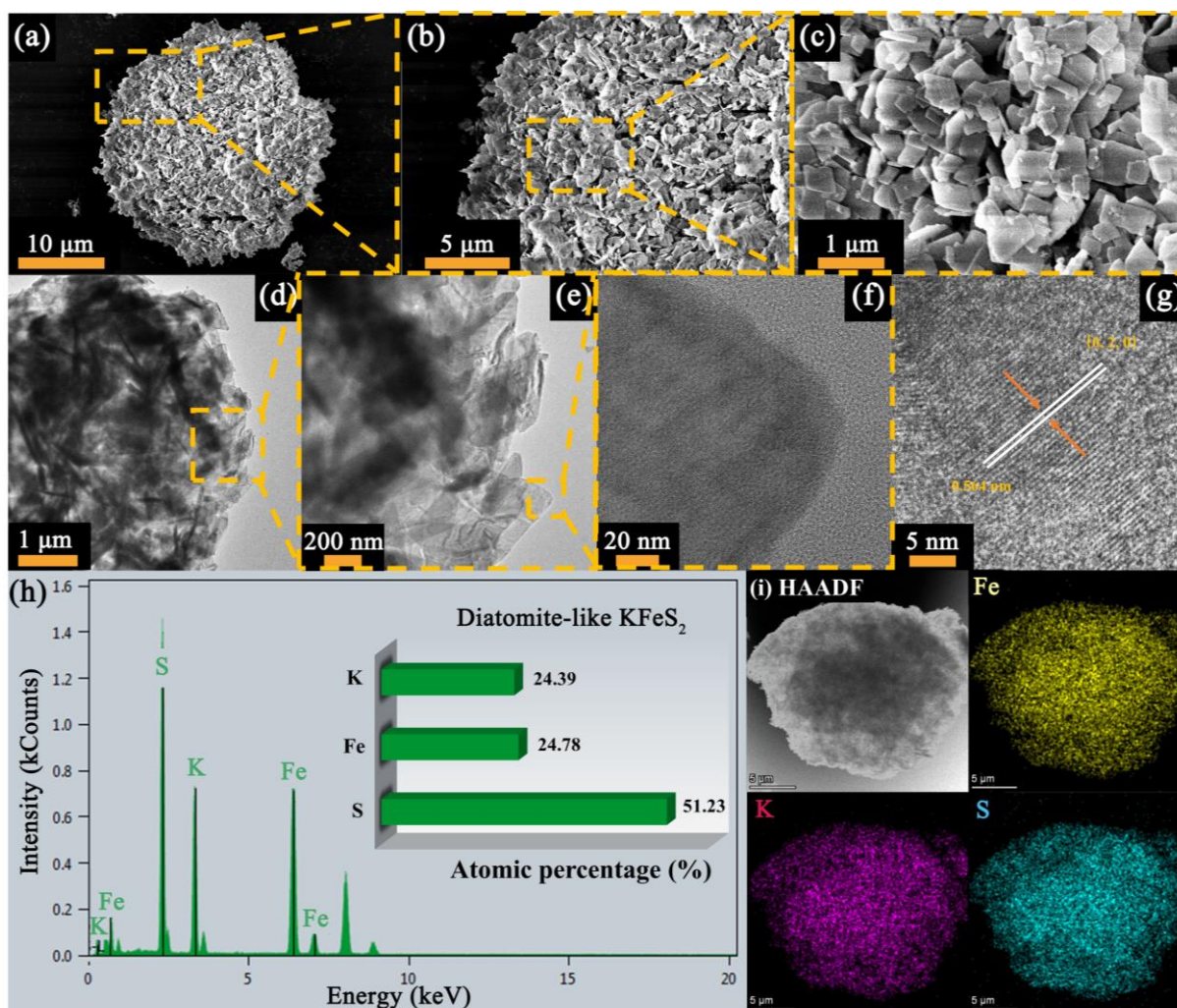


Figure 1. (a–c) Magnification increases for the SEM images of the diatomite-like KFeS_2 ; (d–f) Magnification increases for the TEM images of the diatomite-like KFeS_2 ; (g) Typical TEM image of the diatomite-like KFeS_2 single wire; (h) EDS mapping of diatomite-like KFeS_2 ; (i) HAADF-STEM images and corresponding EDS mapping of diatomite-like KFeS_2 .

The surface properties of the prepared diatomite-like KFeS_2 were tested by Brunauer–Emmett–Teller (BET) and N_2 adsorption–desorption measurements. Figure 2c shows the corresponding N_2 adsorption–desorption isotherms and the pore size distribution curves of the samples. As shown in Figure 2c, the isotherm surface is that of a typical mesoporous material with a sharp increase in N_2 adsorption near a relative pressure of 1, which indicates the presence of macropores in the diatomite-like KFeS_2 . This sharp increase is due to the presence of macropores on the surface of the diatomite template. According to BET analysis, the synthesized diatomite-like KFeS_2 exhibited a large specific surface area of $42.35 \text{ m}^2 \text{ g}^{-1}$, which is much higher than that of the modified diatomite studied in our previous work [35]. From the pore size distribution curves, the diatomite-like KFeS_2 shows a wide pore size spread, and the average pore diameter was 29.03 nm in 4 V A^{-1} by BET, which formed a layered porous structure possessed by the composite. This type of layered surface morphology with good pore structure is beneficial for enhancing the performance of electrochemical capacitors because the large pore channels allow fast electrolyte transport, and the small pores provide more active sites for chemical reactions to take place.

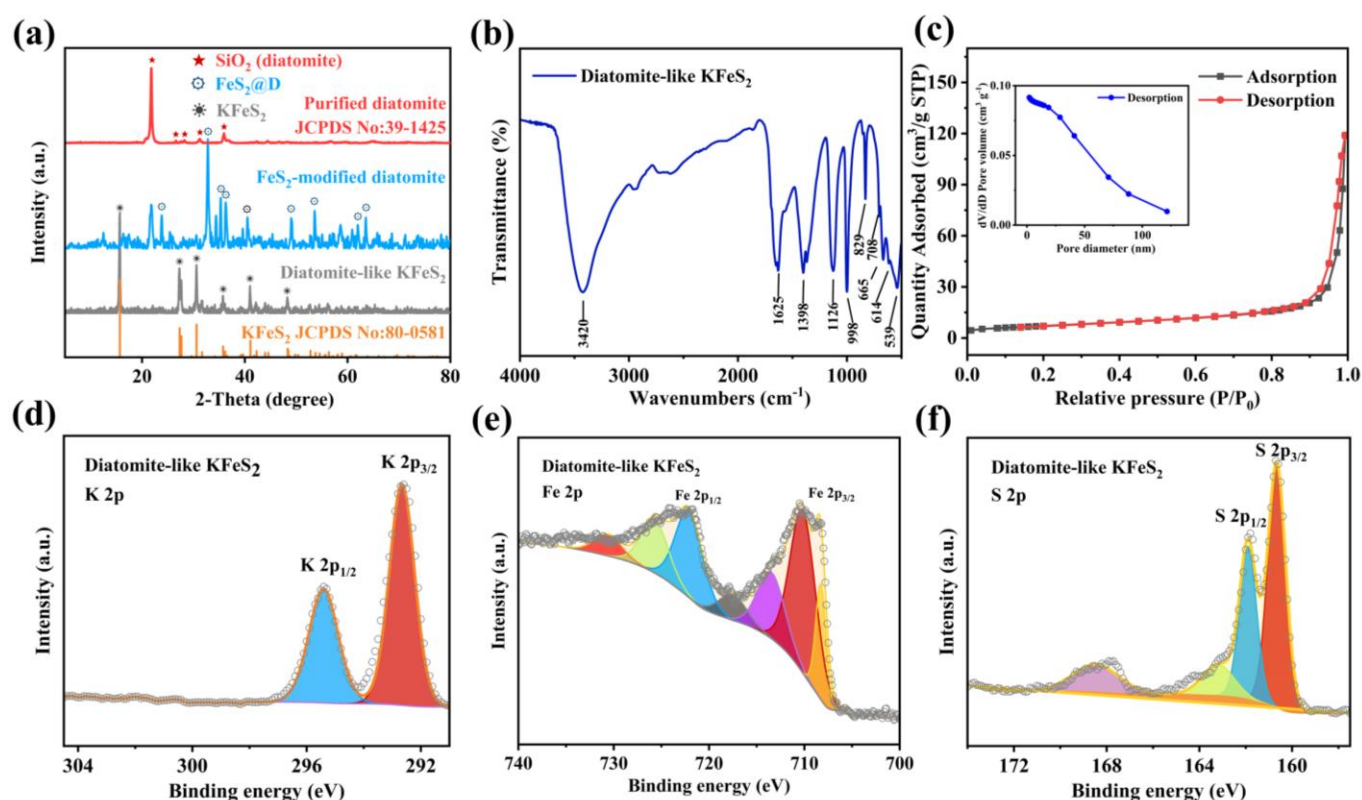


Figure 2. (a) XRD patterns of purified diatomite, KFeS_2 with diatomite morphology, and FeS_2 -modified diatomite; (b) FT-IR spectra of diatomite-like KFeS_2 in the range of 500–4000 cm^{-1} ; (c) N_2 adsorption–desorption isotherms and the corresponding pore size distribution of the diatomite-like KFeS_2 ; high-resolution XPS spectra of K 2p, Fe 2p, and S 2p of the diatomite-like KFeS_2 (d–f), respectively.

To explore the chemical composition of the structure further, X-ray photoelectron spectroscopy (XPS) was performed to examine the elemental states of the diatomite-like KFeS_2 . The corresponding high-resolution spectra of K, Fe, and S are displayed in Figure 2d–f. The XPS spectrum of K 2p in Figure 2d shows two typical peaks at 295.40 eV and 292.61 eV, corresponding to the K 2p_{1/2} and K 2p_{3/2} spin–orbit peaks of diatomite-like KFeS_2 , respectively. Figure 2e shows the spectra of Fe 2p for the diatomite-like KFeS_2 , where the peaks located at binding energies 722.53 eV and 708.32 eV belong to Fe 2p_{1/2} and Fe 2p_{3/2}, respectively, suggesting the presence of Fe^{3+} [36,37]. In Figure 2f, the peaks at 161.81 eV and 160.67 eV correspond to S 2p_{1/2} and S 2p_{3/2}, respectively, and we attribute the additional weak peak at 167.74 eV to a sulfur–oxygen bond that was possibly caused by air contact [38].

Next, in order to compare the electrochemical performance of diatomite-like KFeS_2 , FeS_2 @D, and KFeS_2 , the CV curves at a scan rate of 20 mV s^{-1} with GCD curves at a current density of 4 A g^{-1} are shown in Figure 3a,b. Evidently, the area surrounded by the curve of the diatomite-like KFeS_2 was larger than the others. The GCD curves of the diatomite-like KFeS_2 , FeS_2 @D, and KFeS_2 are shown in Figure 3b. The discharge time of the diatomite-like KFeS_2 was longer than that of FeS_2 @D or KFeS_2 , which indicates its larger capacitance. In addition, the areas of the CV curves of the diatomite-like KFeS_2 and FeS_2 @D were larger than that of KFeS_2 , and their discharge times were also longer than KFeS_2 , indicating enhancement in electrochemical capacitance from diatomite morphology. Additionally, the CV curves of the diatomite-like KFeS_2 electrodes in 6 M KOH aqueous electrolyte at various scan rates are shown in Figure 3c, where an obvious redox peak can be seen that indicates that a typical faradaic pseudo reaction occurred between the KFeS_2 electrode and the KOH electrolyte. As shown in Figure 3d, stable platforms can also be observed in the

charge–discharge curves, indicating a pseudo-reaction response of the active material. The specific capacitance C_m ($F g^{-1}$) can be calculated using Equation (1):

$$C_m = \frac{\int U dt \times I}{0.5m \times \Delta V^2} \quad (1)$$

where I is the discharging current, U is the potential, t is the discharging time, and m is the weight of the active materials. The specific capacitance of diatomite-like $KFeS_2$ was calculated to be $651 F g^{-1}$ at a current density of $1.0 A g^{-1}$, highlighting its unique porous structure and high SSA. High porosity makes it easier for ions to be transferred into the structure, leading to more redox reactions and surface adsorption of electrolyte ions.

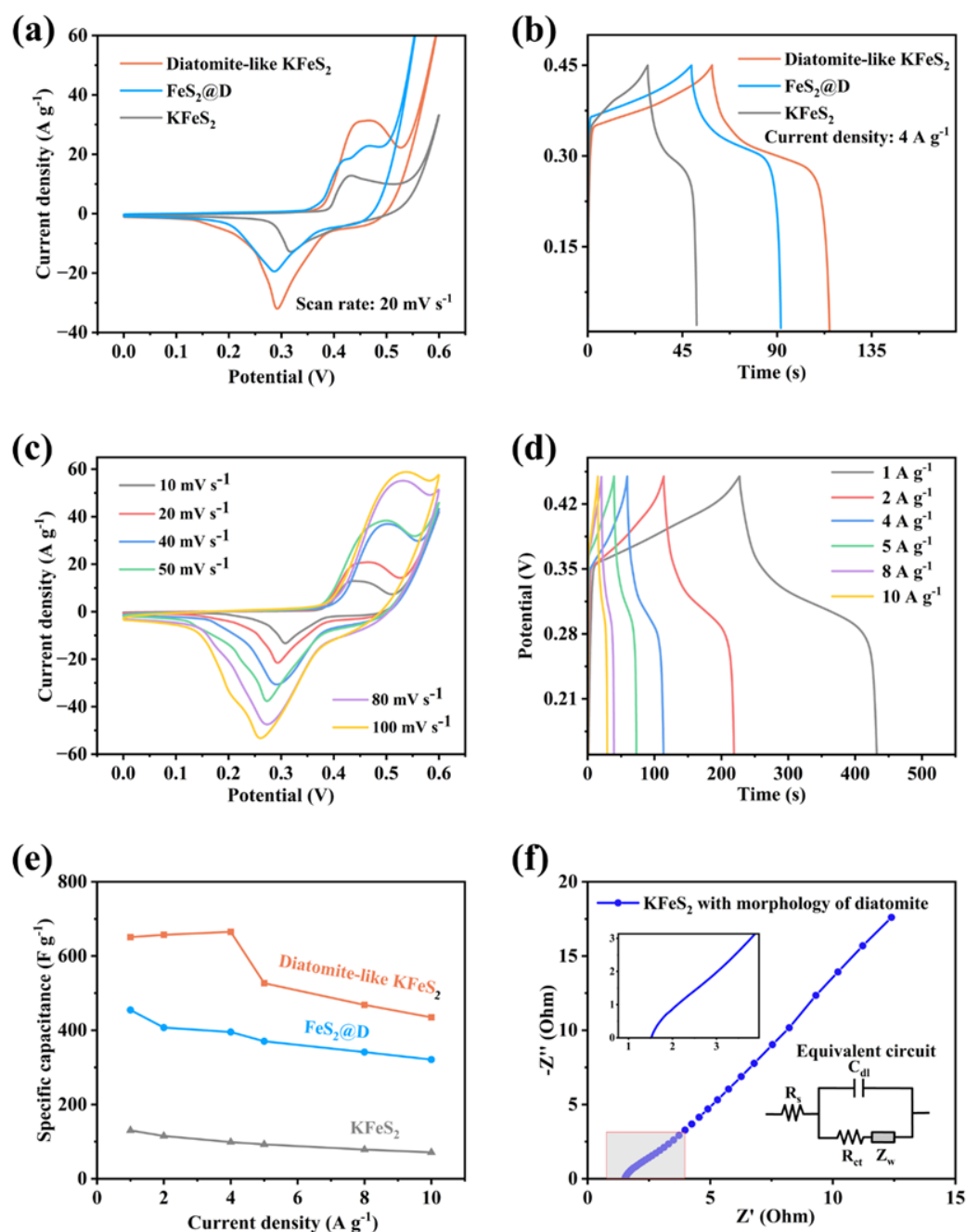


Figure 3. (a) The comparison of cyclic voltammograms at a scan rate of $20 mV s^{-1}$ between diatomite-like $KFeS_2$, $FeS_2@D$, and $KFeS_2$; (b) GCD curves of diatomite-like $KFeS_2$, $FeS_2@D$, and $KFeS_2$ at a current

density of 4 A g^{-1} ; (c) cyclic voltammograms of diatomite-like KFeS_2 composite at different scan rate (10, 20, 40, 50, 80, and 100 mV s^{-1}) in a 6 M KOH aqueous electrolyte; (d) GCD curves of diatomite-like KFeS_2 electrodes at different current densities (1, 2, 4, 5, 8, and 10 mA cm^{-2}); (e) specific capacitances of diatomite-like KFeS_2 , $\text{FeS}_2@D$, and KFeS_2 measured under different current densities; (f) the electrochemical impedance spectrum of the diatomite-like KFeS_2 electrodes at open circuit potential in the frequency range from 0.01 Hz to 100 kHz (the inset is a partial enlargement of the curve).

Table 1 shows the comparison of iron-based sulfide electrodes and highlights the excellent electrochemical performance of diatomite-like KFeS_2 . In addition, the rate capabilities of diatomite-like KFeS_2 , $\text{FeS}_2@D$, and KFeS_2 are displayed in Figure 3e. Obviously, the slope of the diatomite-like KFeS_2 was lower than that of $\text{FeS}_2@D$ or KFeS_2 , meaning that the diatomite-like KFeS_2 had a better rate capability. The overall specific capacitance of the diatomite-like KFeS_2 also showed a slightly decreasing trend as current density increased from 1.0 to 10.0 A g^{-1} . However, a slight increase at low current density (1.0 to 4.0 A g^{-1}) can be ascribed to the thermal effect caused by repeated charging and discharging of the electrode [39]. After increasing the current density to 10 A g^{-1} , about 66.8% of the initial capacitance remained for the diatomite-like KFeS_2 electrode, which serves to highlight its rate capability further. Specifically, this rate in $\text{FeS}_2@D$ was about 70.6% and in KFeS_2 was about 54.6%.

Table 1. Various iron-based sulfide electrode materials with their specific capacitance.

No.	Materials	Morphology	Electrolyte	Specific Capacitance	Reference
1	Diatomite-like KFeS_2	Diatomite-like	6 M KOH	651 F g^{-1} at 1 A g^{-1}	This work
2	FeS_2 CNFs	Nanosphere	6 M KOH	203.4 F g^{-1} at 1 A g^{-1}	[20]
3	Fruit-like $\text{FeS}_2@Carbon$ microspheres	Microsphere	1 M KOH	278.4 F g^{-1} at 1 A g^{-1}	[40]
4	N-doped FeS_2 nanosphere	Nanosphere	0.5 M NaOH	238.2 mF g^{-1} at 3 mA g^{-1}	[41]
5	50% $\text{FeS}_2/3\text{DPCC}$ (FeS_2 content at 50% weight percent)	Nanoparticles	1 M KOH	304 F g^{-1} at 2 A g^{-1}	[30]
6	Donator- FeS/C	Nanoparticles	2 M KOH	275.65 F g^{-1} at 30 mA cm^{-2}	[42]
7	$\text{FeS}_2/PVP/NF$	Nanoparticles	3 M KOH	526.08 F g^{-1} at 1 A g^{-1}	[12]
8	FeS_x grown on stainless steel	Cuboidal-like	$1 \text{ M Na}_2\text{SO}_4$	730 mF g^{-1} at 1 mA g^{-1}	[43]
9	Hierarchical $\text{FeS}/\text{RGO}/\text{FeS}@Fe$ foil	Nanosheets	2 M KOH	206.25 F g^{-1} at 20 mA cm^{-2}	[44]

The rate capabilities of the diatomite-like KFeS_2 and $\text{FeS}_2@D$ were both better than KFeS_2 , which indicates improvement from introducing the diatomite morphology. Furthermore, Figure S1 shows the cycle performance of the diatomite-like KFeS_2 at a current density of 4 A g^{-1} . Here, we see that the impedance of the diatomite-like KFeS_2 electrode was calculated over a frequency range of 100 kHz – 0.01 Hz by applying an AC voltage with an amplitude of 5 mV at the open circuit potential. As shown in Figure 3f, the impedance patterns had a half arc at high frequencies and a linear part at low frequencies. The equivalent circuit of the Nyquist plot is shown in Figure 3f, where we can see that the impedance arc in the high frequencies region can be replaced by an interfacial Faraday charge transfer resistor (R_{ct}) and a parallel constant phase element (C_d) for the double layer capacitance. A straight line with a slope of 45° in the mid-frequency region along the arc indicates the finite-length diffusive Warburg impedance (Z_w), which is associated with the diffusion/transport of electrolyte ions in the electrode. The vertical line in the very low frequency region shows the ideal capacitive behavior of the diatomite-like KFeS_2 electrode material, and the EIS results show the pseudo-capacitive properties and porous structure characteristics of the diatomite-like KFeS_2 electrode.

The catalytic performance of the diatomite-like KFeS_2 was also evaluated in 1 M KOH . For comparison, FeS_2 -modified diatomite and iron-based sulfide without diatomite morphology (KFeS_2) were set as controls. The electrocatalytic activities of the diatomite-like

KFeS₂, FeS₂@D, and KFeS₂ nanostructured electrodes were investigated using linear sweep voltammetry (LSV) measurements at a scan rate of 5.0 mA s⁻¹, and the results are shown in Figure 4a. The overpotential (η) for the diatomite-like KFeS₂ was estimated to be ~0.25 mV, which was much lower than both KFeS₂ (~0.29 mV) and FeS₂@D (~0.37 mV at a current density of 10 mA cm⁻²). In addition, the Tafel slopes of the diatomite-like KFeS₂, KFeS₂, and FeS₂@D were estimated as 48.4 mV dec⁻¹, 52.7 mV dec⁻¹, and 155.4 mV dec⁻¹, respectively, as shown in Figure 4b. The Tafel slope of the diatomite-like KFeS₂ was lower than the other two structures, indicating its superior reaction kinetics characteristics and excellent oxygen evolution performance. The EIS impedance spectrum in Figure 4c also shows that the impedance of the diatomite-like KFeS₂ was much lower than that of KFeS₂ or FeS₂@D, which indicates its superior electrical conductivity. The lowest impedance of diatomite-like KFeS₂ favors the transfer of electrons and results in the lowest overpotential among the three substances as well. This low impedance is also beneficial for the adsorption and desorption of intermediates during the reaction process and contributes to the excellent catalytic performance of diatomite-like KFeS₂.

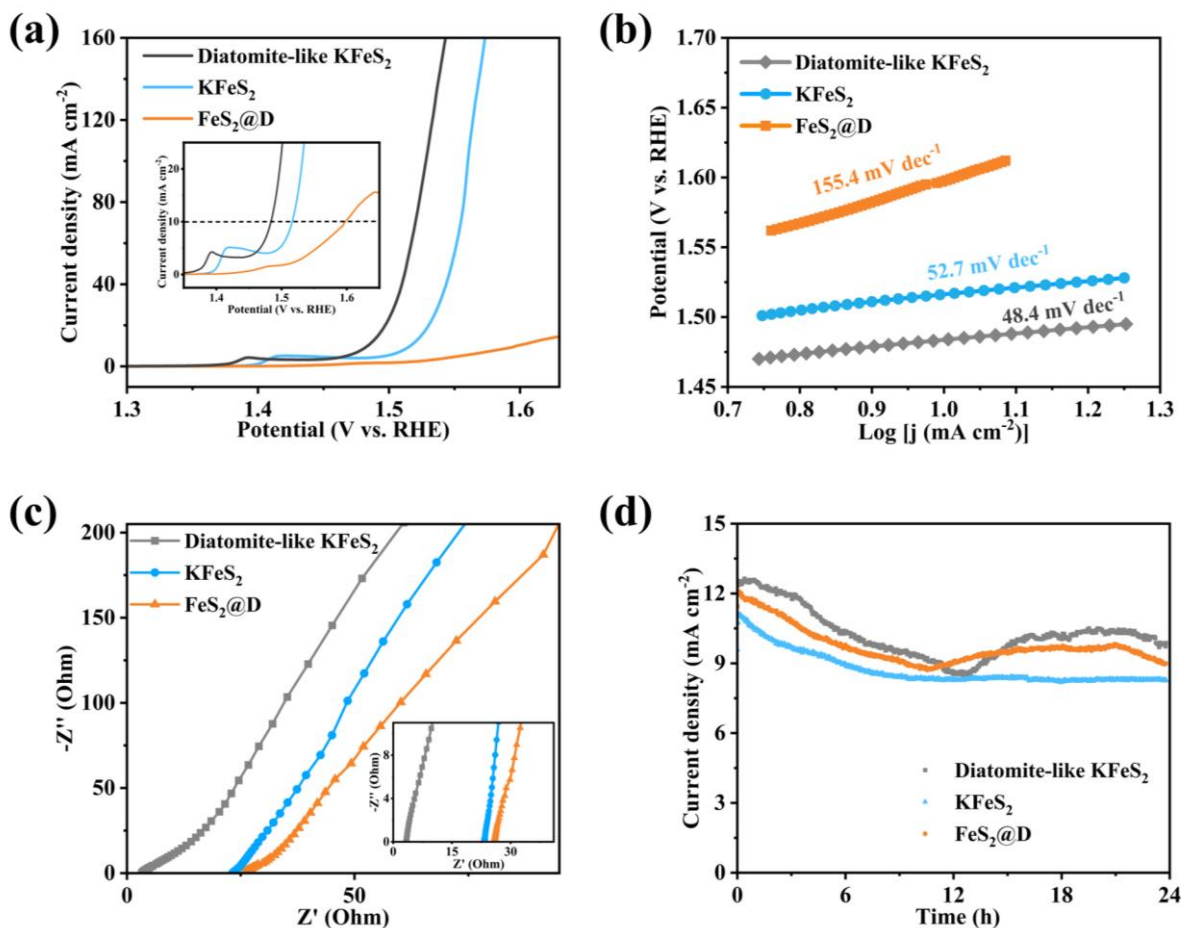


Figure 4. (a) LSV plots (the inset is the partial enlargement plot); (b) the corresponding Tafel plots; (c) comparison of EIS between diatomite-like KFeS₂, KFeS₂, and FeS₂@D (the partial enlargement plot is shown in the inset); (d) current–time curves of diatomite-like KFeS₂, KFeS₂, and FeS₂@D for 24 h.

Cycling performance was further tested using the time–current method, and the results for the diatomite-like KFeS₂, KFeS₂, and FeS₂@D at an initial potential of 0.53 V, 0.62 V, and 0.67 V for each after 24 h are shown in Figure 4d. Analysis of the time–current curve results shows that the cycling stability of the diatomite-like KFeS₂ and FeS₂@D were much higher than that of the KFeS₂ without the morphology of diatomite. The cyclic curves of the

diatomite-like KFeS_2 and $\text{FeS}_2@D$ were noticeably similar, indicating that the morphology of diatomite made a central contribution to its cycling performance.

The electrocatalytic performance of catalysts for hydrolysis is highly dependent on their catalytic activity and the number of active sites, which are closely related to the morphology, size, and structure of the catalyst [45]. Indeed, we found that the extremely low overpotential, good electrical conductivity, and superior cycling stability of the diatomite-like KFeS_2 synthesized in this study were due to its unique diatomite nanostructure, which increased the number of active centers. According to the adsorbate evolution mechanism (AEM), an increased number of metal active sites can adsorb more intermediates and can facilitate the synergistic effect of Fe and S, thus accelerating the electrocatalytic performance of water decomposition [46]. Finally, we provide a table of comparisons (see Table 2) of the results for the diatomite-like KFeS_2 with other sulfides that have been reported earlier, and these results show that the prepared diatomite-like KFeS_2 had excellent OER performance.

Table 2. Various iron-based sulfide electrode materials with their Tafel slopes and overpotentials.

No.	Materials	Morphology	Tafel Slope (mV dec ⁻¹)	Overpotential (mV)	Reference
1	Diatomite-like KFeS_2	Diatomite-like	48.4	254@10 mA cm ⁻²	This work
2	$\text{FeNi(OH)}_x/\text{FeS}/\text{IF}$	Nanosheets	53	273@10 mA cm ⁻²	[47]
3	$\text{FeS}/\text{Fe}_2\text{O}_3$ heterogeneous nanosheets	Nanosheets	51.71	266.5@10 mA cm ⁻²	[16]
4	$\text{Fe}_2\text{O}_3/\text{FeS}$	Nanorods	90	370@40 mA cm ⁻²	[15]
5	Hybrid nanoarray	Nanoarray	80	260@10 mA cm ⁻²	[14]
6	$\text{FeS-Co}_9\text{S}_8/\text{IF}$	Heterostructure	50.3	332@500 mA cm ⁻²	[48]
7	FeS	-	69	320@10 mA cm ⁻²	[49]
8	FeS_x/CF	Heterostructure	105	340@10 mA cm ⁻²	[50]
9	$\text{FeS}_2@\text{MXene}$	Nanoparticles	58.6	240@10 mA cm ⁻²	[51]

4. Conclusions

In summary, diatomite-like KFeS_2 was successfully synthesized using a simple multi-step sacrificial template method. The nanostructure exhibited the potential for a broad set of applications, such as in supercapacitor anodes and electrocatalysts for OERs. The diatomite-like KFeS_2 also exhibited extremely high specific capability (651 F g⁻¹ at 1.0 A g⁻¹). In addition, as an electrocatalyst, the diatomite-like KFeS_2 possessed a lower overpotential (η_{10} of 254 mV at a current density of 10 mA cm⁻²) during OERs, compared to other iron-based sulfide composite materials. These results indicate that diatomite-like KFeS_2 shows promise for use in the assembly of supercapacitors and oxygen precipitation reactions.

Supplementary Materials: The following supporting information can be downloaded at: <https://www.mdpi.com/article/10.3390/nano13040643/s1>, Figure S1: Cycle performance of diatomite-like KFeS_2 .

Author Contributions: Conceptualization and methodology, K.L., C.W., Q.S. and Y.Z. (Yuxin Zhang); experiment, C.W., K.L., Y.Z. (Yunhao Zhang), Z.S., C.Z. and Y.H.; data curation, C.W., Q.S. C.Z. and K.L.; writing—original draft preparation, C.W. and S.Z.; writing—review and editing, S.Z., C.W., Q.S., K.L. and Y.Z. (Yuxin Zhang). All authors have read and agreed to the published version of the manuscript.

Funding: This research was funded by the National Natural Science Foundation of China (Grant No. 51908092), Projects (No. 2020CDJXZ001, 2021CDJMRH-005 and SKLMT-ZZKT-2021M04) supported by the Fundamental Research Funds for the Central Universities, the Joint Funds of the National Natural Science Foundation of China-Guangdong (Grant No. U1801254), the project funded by Chongqing Special Postdoctoral Science Foundation (XmT2018043), the Chongqing Research Program of Basic Research and Frontier Technology (cstc2017jcyjBX0080), the Natural Science Foundation Project of Chongqing for Post-doctor (cstc2019jcyjbs0079 and cstc2019jcyjbsX0085), Technological Projects of Chongqing Municipal Education Commission (KJZDK201800801), the Innovative Research

Team of Chongqing (CXTDG201602014), and Innovative Technology of New Materials and Metallurgy (2019CDXYCL0031).

Institutional Review Board Statement: Not applicable.

Informed Consent Statement: Not applicable.

Data Availability Statement: Data of the compounds are available from the authors.

Acknowledgments: The authors also gratefully acknowledge the Electron Microscopy Center of Chongqing University for materials characterization.

Conflicts of Interest: The authors declare no conflict of interest.

References

1. Kim, J.; Lee, J.; Liu, C.; Pandey, S.; Joo, S.W.; Son, N.; Kang, M. Achieving a long-term stability by self-redox property between Fe and Mn ions in the iron-manganese spinel structured electrode in oxygen evolution reaction. *Appl. Surf. Sci.* **2021**, *546*, 149124. [[CrossRef](#)]
2. Liu, J.H.; He, X.; Wang, Y.Y.; Sun, Z.J.; Liu, Y.S.; Liu, B.S.; Li, H.D.; Guo, F.; Li, X. Deep reconstruction of highly disordered iron/nickel nitrate hydroxide nanoplates for high-performance oxygen evolution reaction in alkaline media. *J. Alloy. Compd.* **2022**, *927*, 167060. [[CrossRef](#)]
3. Zhang, G.G.; Yuan, J.Y.; Liu, Y.; Lu, W.; Fu, N.Q.; Li, W.F.; Huang, H.T. Boosting the oxygen evolution reaction in non-precious catalysts by structural and electronic engineering. *J. Mater. Chem. A* **2018**, *6*, 10253–10263. [[CrossRef](#)]
4. Wang, C.H.; Li, C.M.; Liu, J.L.; Guo, C.X. Engineering transition metal-based nanomaterials for high-performance electrocatalysis. *Mater. Rep. Energy* **2021**, *1*, 100006. [[CrossRef](#)]
5. Chen, W.; Rakhi, R.B.; Hu, L.B.; Xie, X.; Cui, Y.; Alshareef, H.N. High-Performance Nanostructured Supercapacitors on a Sponge. *Nano Lett.* **2011**, *11*, 5165–5172. [[CrossRef](#)] [[PubMed](#)]
6. Zhang, Y.X.; Huang, M.; Li, F.; Wang, X.L.; Wen, Z.Q. One-pot synthesis of hierarchical MnO₂-modified diatomites for electrochemical capacitor electrodes. *J. Power Sources* **2014**, *246*, 449–456. [[CrossRef](#)]
7. Simon, P.; Gogotsi, Y. Materials for electrochemical capacitors. *Nat. Mater.* **2008**, *7*, 845–854. [[CrossRef](#)] [[PubMed](#)]
8. Zeng, Y.; Yu, M.; Meng, Y.; Fang, P.; Lu, X.; Tong, Y. Iron-Based Supercapacitor Electrodes: Advances and Challenges. *Adv. Energy Mater.* **2016**, *6*, 1601053. [[CrossRef](#)]
9. Owusu, K.A.; Qu, L.; Li, J.; Wang, Z.; Zhao, K.; Yang, C.; Hercule, K.M.; Lin, C.; Shi, C.; Wei, Q.; et al. Low-crystalline iron oxide hydroxide nanoparticle anode for high-performance supercapacitors. *Nat. Commun.* **2017**, *8*, 14264. [[CrossRef](#)]
10. Bu, R.R.; Deng, Y.; Wang, Y.L.; Zhao, Y.; Shi, Q.Q.; Zhang, Q.; Xiao, Z.Y.; Li, Y.Y.; Sun, W.; Wang, L. Bucket Effect: A Metal-Organic Framework Derived High-Performance FeS₂/Fe₂O₃@S-rGO Negative Material for Enhanced Overall Supercapacitor Capacitance. *ACS Appl. Energy Mater.* **2021**, *4*, 11004–11013. [[CrossRef](#)]
11. Chen, X.L.; Shi, T.; Zhong, K.L.; Wu, G.L.; Lu, Y. Capacitive behavior of MoS₂ decorated with FeS₂@carbon nanospheres. *Chem. Eng. J.* **2020**, *379*, 122240. [[CrossRef](#)]
12. Durga, I.K.; Rao, S.S.; Kalla, R.M.N.; Ahn, J.W.; Kim, H.J. Facile synthesis of FeS₂/PVP composite as high-performance electrodes for supercapacitors. *J. Energy Storage* **2020**, *28*, 101216. [[CrossRef](#)]
13. Pham, D.T.; Baboo, J.P.; Song, J.; Kim, S.; Mathew, V.; Alfaruqi, M.H.; Sambandam, B.; Kim, J. Facile synthesis of pyrite (FeS₂/C) nanoparticles as an electrode material for non-aqueous hybrid electrochemical capacitors. *Nanoscale* **2018**, *10*, 5938–5949. [[CrossRef](#)] [[PubMed](#)]
14. Luan, X.Q.; Du, H.T.; Kong, Y.; Qu, F.L.; Lu, L.M. A novel FeS-NiS hybrid nanoarray: An efficient and durable electrocatalyst for alkaline water oxidation. *Chem. Commun.* **2019**, *55*, 7335–7338. [[CrossRef](#)]
15. Khan, N.A.; Rashid, N.; Ahmad, I.; Zahidullah; Zairov, R.; Rehman, H.U.; Nazar, M.F.; Jabeen, U. An efficient Fe₂O₃/FeS heterostructures water oxidation catalyst. *Int. J. Hydrog. Energy* **2022**, *47*, 22340–22347. [[CrossRef](#)]
16. Guo, W.H.; Zhang, Q.; Fu, H.C.; Yang, Y.X.; Chen, X.H.; Luo, H.Q.; Li, N.B. Semi-sacrificial template growth of FeS/Fe₂O₃ heterogeneous nanosheets on iron foam for efficient oxygen evolution reaction. *J. Alloy. Compd.* **2022**, *909*, 164670. [[CrossRef](#)]
17. Xue, Y.R.; Liu, M.Y.; Qin, Y.Y.X.; Zhang, Y.F.; Zhang, X.J.; Fang, J.J.; Zhang, X.; Zhu, W.; Zhuang, Z.B. Ultrathin NiFeS nanosheets as highly active electrocatalysts for oxygen evolution reaction. *Chin. Chem. Lett.* **2022**, *33*, 3916–3920. [[CrossRef](#)]
18. Feng, D.; Zhang, X.; Sun, Y.; Ma, T. Surface-defective FeS₂ for electrochemical NH₃ production under ambient conditions. *Nano Mater. Sci.* **2020**, *2*, 132–139. [[CrossRef](#)]
19. Huang, F.; Wu, R.; Li, J.; Sun, Y.F.; Jian, J.K. *Synthesis of NaFeS₂ Nanorods by Solvothermal Technique, International Forum on Mechanical and Material Engineering (IFMME 2013)*; Trans Tech Publications Ltd.: Guangzhou, China, 2013; pp. 603–608.
20. Huang, Y.; Zhao, H.; Bao, S.; Yin, Y.; Zhang, Y.; Lu, J. Hollow FeS₂ nanospheres encapsulated in N/S co-doped carbon nanofibers as electrode material for electrochemical energy storage. *J. Alloy. Compd.* **2022**, *905*, 164184. [[CrossRef](#)]
21. Li, L.X.; Gao, T.Y.; Ge, Y.S.; Zhang, Q.; Wang, J.Y.; Ma, Z.P.; Guo, W.F.; Yu, S.X.; Fan, Y.Q. Ultra-long KFeS₂ nanowires grown on Fe foam as a high-performance anode for aqueous solid-state energy storage. *J. Mater. Chem. A* **2021**, *9*, 27727–27735. [[CrossRef](#)]

22. Liang, D.X.; Ji, M.H.; Zhu, S.Y.; Chen, Y.; Wang, Z.H.; Liu, Y.W.; Khan, A.H.R.; Ri, Y.H.; Yu, H.B.; Huo, M.X. A novel Fe recycling method from pickling wastewater producing a KFeS₂ whisker for electroplating wastewater treatment. *Environ. Sci. Wat. Res. Technol.* **2021**, *7*, 1480–1491. [[CrossRef](#)]
23. Tufa, L.T.; Gicha, B.B.; Wu, H.; Lee, J. Fe-Based Mesoporous Nanostructures for Electrochemical Conversion and Storage of Energy. *Batter. Supercaps* **2021**, *4*, 429–444. [[CrossRef](#)]
24. Yang, J.; Chen, J.W.; Wang, Z.X.; Wang, Z.; Zhang, Q.C.; He, B.; Zhang, T.; Gong, W.B.; Chen, M.X.; Qi, M.; et al. High-Capacity Iron-Based Anodes for Aqueous Secondary Nickel-Iron Batteries: Recent Progress and Prospects. *Chem. Electro. Chem.* **2021**, *8*, 274–290.
25. Fang, Y.J.; Chen, Z.X.; Xiao, L.F.; Ai, X.P.; Cao, Y.L.; Yang, H.X. Recent Progress in Iron-Based Electrode Materials for Grid-Scale Sodium-Ion Batteries. *Small* **2018**, *14*, 1703116. [[CrossRef](#)] [[PubMed](#)]
26. Li, B.; Pang, H.; Xue, H.G. Fe-based phosphate nanostructures for supercapacitors. *Chin. Chem. Lett.* **2021**, *32*, 885–889. [[CrossRef](#)]
27. Wu, X.Y.; Markir, A.; Xu, Y.K.; Zhang, C.; Leonard, D.P.; Shin, W.; Ji, X.L. A Rechargeable Battery with an Iron Metal Anode. *Adv. Funct. Mater.* **2019**, *29*, 1900911. [[CrossRef](#)]
28. Jayathilake, B.S.; Plichta, E.J.; Hendrickson, M.A.; Narayanan, S.R. Improvements to the Coulombic Efficiency of the Iron Electrode for an All-Iron Redox-Flow Battery. *J. Electrochem. Soc.* **2018**, *165*, A1630–A1638. [[CrossRef](#)]
29. Liu, W.W.; Zhu, M.H.; Liu, J.H.; Li, X.; Liu, J. Flexible asymmetric supercapacitor with high energy density based on optimized MnO₂ cathode and Fe₂O₃ anode. *Chin. Chem. Lett.* **2019**, *30*, 750–756. [[CrossRef](#)]
30. Wu, Z.-S.; Sun, Y.; Tan, Y.-Z.; Yang, S.; Feng, X.; Muellen, K. Three-Dimensional Graphene-Based Macro- and Mesoporous Frameworks for High-Performance Electrochemical Capacitive Energy Storage. *J. Am. Chem. Soc.* **2012**, *134*, 19532–19535. [[CrossRef](#)]
31. Yu, Y.; Addai-Mensah, J.; Losic, D. Synthesis of Self-Supporting Gold Microstructures with Three-Dimensional Morphologies by Direct Replication of Diatom Templates. *Langmuir* **2010**, *26*, 14068–14072. [[CrossRef](#)]
32. Dai, X.; Rao, J.; Bao, Z.; Li, K.; Feng, L.; Song, D.; Zhao, L.; Li, W.; Liu, X.; Yi, S.; et al. Magnetic double-core@shell MnO₂@NiFe@DE as a multifunctional scavenger for efficient removal of tetracycline, anionic and cationic dyes. *J. Colloid Interface Sci.* **2022**, *628*, 769–783. [[CrossRef](#)]
33. Li, K.; Teng, H.; Sun, Q.; Li, Y.; Wu, X.; Dai, X.; Wang, Y.; Wang, S.; Zhang, Y.; Yao, K.; et al. Engineering active sites on nitrogen-doped carbon nanotubes/cobaltic oxide heterostructure embedded in biotemplate for high-performance supercapacitors. *J. Energy Storage* **2022**, *53*, 105094. [[CrossRef](#)]
34. Philiat, J.M.; Marsan, B. FTIR spectroscopic study and thermal and electrical properties of polymer electrolytes containing a cesium thiolate/disulfide redox couple. *Electrochim. Acta* **1999**, *44*, 2351–2363. [[CrossRef](#)]
35. Sprynskyy, M.; Gadzala-Kopciuch, R.; Nowak, K.; Buszewski, B. Removal of zearalenone toxin from synthetics gastric and body fluids using talc and diatomite: A batch kinetic study. *Colloids Surf. B* **2021**, *94*, 7–14. [[CrossRef](#)] [[PubMed](#)]
36. Ni, J.F.; Sun, M.L.; Li, L. Highly Efficient Sodium Storage in Iron Oxide Nanotube Arrays Enabled by Built-In Electric Field. *Adv. Mater.* **2019**, *31*, 1902603. [[CrossRef](#)] [[PubMed](#)]
37. Wang, M.X.; Wang, L.S.; Yue, G.H.; Wang, X.; Yan, P.X.; Peng, D.L. Single crystal of CuFeS₂ nanowires synthesized through solventothermal process. *Mater. Chem. Phys.* **2009**, *115*, 147–150. [[CrossRef](#)]
38. Yang, J.; Zhang, Q.C.; Wang, Z.X.; Wang, Z.; Kang, L.X.; Qi, M.; Chen, M.X.; Liu, W.; Gong, W.B.; Lu, W.B.; et al. Rational Construction of Self-Standing Sulfur-Doped Fe₂O₃ Anodes with Promoted Energy Storage Capability for Wearable Aqueous Rechargeable NiCo-Fe Batteries. *Adv. Energy Mater.* **2020**, *10*, 2001064. [[CrossRef](#)]
39. Wang, K.; Wang, J.; Wu, Y.; Zhao, S.; Wang, Z.; Wang, S. Millisecond photo-thermal process on significant improvement of supercapacitor's performance. *Appl. Therm. Eng.* **2016**, *109*, 186–195. [[CrossRef](#)]
40. Liu, X.X.; Deng, W.Z.; Liu, L.M.; Wang, Y.F.; Huang, C.F.; Wang, Z.J. Passion fruit-like microspheres of FeS₂ wrapped with carbon as an excellent fast charging material for supercapacitors. *New J. Chem.* **2022**, *46*, 11212–11219. [[CrossRef](#)]
41. Wang, Q.; Liu, Q.Q.; Ni, Y.L.; Yang, Y.; Zhu, X.F.; Song, Y. N-Doped FeS₂ Achieved by Thermal Annealing of Anodized Fe in Ammonia and Sulfur Atmosphere: Applications for Supercapacitors. *J. Electrochem. Soc.* **2021**, *168*, 080522. [[CrossRef](#)]
42. Cai, J.; Lai, C.L.; Sun, P.X.; Cui, B.L.; Yang, C. 3 electrons donator-FeS/C composite anode for supercapacitor. *J. Mater. Sci. Mater. Electron.* **2022**, *33*, 26966–26979. [[CrossRef](#)]
43. Shao, X.X.; Zhu, Z.Q.; Zhao, C.J.; Zhao, C.H.; Qian, X.Z. Hierarchical FeS/RGO/FeS@Fe foil as high-performance negative electrode for asymmetric supercapacitors. *Inorg. Chem. Front.* **2018**, *5*, 1912–1922. [[CrossRef](#)]
44. Upadhyay, K.K.; Nguyen, T.; Silva, T.M.; Carmezim, M.J.; Montemor, M.F. Pseudocapacitive behaviour of FeS_x grown on stainless steel up to 1.8 V in aqueous electrolyte. *J. Energy Storage* **2019**, *26*, 100949. [[CrossRef](#)]
45. Zhang, K.; Zou, R. Advanced Transition Metal-Based OER Electrocatalysts: Current Status, Opportunities, and Challenges. *Small* **2021**, *17*, 2100129. [[CrossRef](#)] [[PubMed](#)]
46. Song, J.; Wei, C.; Huang, Z.-F.; Liu, C.; Zeng, L.; Wang, X.; Xu, Z.J. A review on fundamentals for designing oxygen evolution electrocatalysts. *Chem. Soc. Rev.* **2020**, *49*, 2196–2214. [[CrossRef](#)]
47. Chen, Q.W.; Zhang, X.Y.; Dong, Y.W.; Guo, B.Y.; Ma, Y.; Wang, L.; Lv, R.Q.; Zhou, Y.L.; Chai, Y.M.; Dong, B. Ultrafast surface modification of FeS nanosheet arrays with Fe-Ni bimetallic hydroxides for efficient oxygen evolution. *J. Alloy. Compd.* **2020**, *835*, 155298. [[CrossRef](#)]

48. Liu, H.J.; Yu, N.; Yuan, X.Q.; Zhao, H.Y.; Zhang, X.Y.; Chai, Y.M.; Dong, B. 0D-2D Schottky heterostructure coupling of FeS nanosheets and Co₉S₈ nanoparticles for long-term industrial-level water oxidation. *Nano Res.* **2022**. [[CrossRef](#)]
49. Shankar, A.; Elakkiya, R.; Maduraiveeran, G. Self-supported fabrication and electrochemical water splitting study of transition-metal sulphide nanostructured electrodes. *New J. Chem.* **2020**, *44*, 5071–5078. [[CrossRef](#)]
50. Wang, W.B.; Xu, R.D.; Yu, B.H.; Wang, X.B.; Feng, S.Y. Electrochemical fabrication of FeS_x films with high catalytic activity for oxygen evolution. *Rsc Adv.* **2019**, *9*, 31979–31987. [[CrossRef](#)]
51. Xie, Y.Y.; Yu, H.Z.; Deng, L.M.; Amin, R.S.; Yu, D.S.; Fetohi, A.E.; Maximov, M.Y.; Li, L.L.; El-Khatib, K.M.; Peng, S.J. Anchoring stable FeS₂ nanoparticles on MXene nanosheets via interface engineering for efficient water splitting. *Inorg. Chem. Front.* **2022**, *9*, 662–669. [[CrossRef](#)]

Disclaimer/Publisher's Note: The statements, opinions and data contained in all publications are solely those of the individual author(s) and contributor(s) and not of MDPI and/or the editor(s). MDPI and/or the editor(s) disclaim responsibility for any injury to people or property resulting from any ideas, methods, instructions or products referred to in the content.